Spin dynamics and exchange interaction in orthoferrite TbFeO₃ with non-Kramers rare-earth ion

S. A. Skorobogatov,[1,2] K. A. Shaykhutdinov,[1,2,*] D. A. Balaev,[1,2] M. S. Pavlovskii,[1,2] A. A. Krasikov,[1] and K. Yu. Terentjev[1]

[1]*Kirensky Institute of Physics, Federal Research Center KSC SB RAS, Krasnoyarsk, 660036 Russia*
[2]*Siberian Federal University, Krasnoyarsk 660041, Russia*

The low-temperature spin dynamics of the orthorhombic TbFeO₃ perovskite has been studied. It has been found that the inelastic neutron scattering (INS) spectrum of the investigated compound contains two modes corresponding to different sublattices. It is shown that the iron subsystem orders antiferromagnetically at $T_N = 632$ K and exhibits the high-energy magnon dispersion. The magnetic dynamics of this subsystem has been described within the linear spin wave theory and the in-plane and out-of-plane exchange anisotropy has been demonstrated. The approach proposed previously to describe the magnon dispersion in the TmFeO₃ compound has been used. Three levels of the nondispersive crystal electric field corresponding to Tb³⁺ ions have been found in the energy region below 40 meV at about 17, 26, and 35 meV. The behavior of the magnetic correlation length of the terbium subsystem has been determined by studying the diffuse scattering at different temperatures. The evolution of this subsystem has been numerically described within the point charge model. It is shown that the numerical data agree satisfactorily with the experiment and with the general concept of the single-ion approximation applied to the rare-earth subsystem of orthorhombic perovskites.

I. INTRODUCTION

The magnetic oxide materials containing transition and rare-earth ions exhibit a diversity of intriguing properties related to the complex interaction between two magnetic subsystems. Among such materials are manganites with the general formulas RMnO₃ [1,2] and RMn₂O₅ [3,4] and huntites RFe₃(BO₃)₄ [5–8]. A separate class of the oxide compounds are RFeO₃ orthoferrites [9], which have been explored for the last few decades [10–12]. The RFeO₃ crystal structure is described by sp. gr. *Pbnm*. The recent renewed interest in these compounds is due to the discovery of several curious phenomena, including multiferroism below the temperature of ordering of the rare-earth subsystem [13], laser-induced ultrafast magnetization switching of domain walls [14–16], and the formation of a soliton lattice in the TbFeO₃ compound [17].

The family of rare-earth orthoferrites attracts attention by intriguing magnetic phenomena. The unique magnetic properties of these compounds are induced by complex interactions between the $3d$ and $4f$ electron magnetic moments. As shown in [9], the RFeO₃ compounds have the extraordinarily high Néel temperatures ($T_N \approx 600$–700 K), below which the moments of iron ions are ordered antiferromagnetically with a weak sublattice canting resulting in weak ferromagnetism. As the temperature decreases, the Fe-R coupling strengthens and induces spin-reorientation transitions at temperatures of $T \ll T_N$. The temperature T_{SR} of the spin-reorientation transition depends strongly on a rare-earth ion. In particular, in the HoFeO₃ compound, this temperature is $T_{SR} \approx 50$–60 K; for TmFeO₃ it is $T_{SR} \approx 80$–90 K [18]; and, with Tb as a rare-earth

element, it is much lower: $T_{SR} \approx 3$–10 K [17,19]. At high temperatures, the subsystem of rare-earth ions with a relatively weak R-R coupling is paramagnetic or weakly polarized by the molecular field of ordered Fe ions. The complex magnetic properties of the rare-earth subsystem are determined by the diversity of exchange interactions. Here, along with the Heisenberg-type Fe-Fe, Fe-R, and R-R exchange interactions, an important role is played by the Dzyaloshinskii-Moriya (DMI) interaction [20], which induces a weak ferromagnetic moment.

In [21], several orthoferrites were investigated and isostructural perovskite compounds containing different rare-earth ions were examined by inelastic neutron scattering (INS), a basic tool for studying energy excitation spectra of magnetic subsystems. In the YbFeO₃ single crystal [22], the quasi-one-dimensional Yb³⁺ chains and "shadow modes" in the low-temperature spin dynamics of the rare-earth subsystem were found. A shadow mode is the phenomenon of the coexistence of two magnon dispersion branches of identical shapes and similar intensities, which are shifted relative to each other by half a period. This effect is possibly induced by buckling of magnetic chains; at $\mathbf{k} = 0$ there is no shadow mode and its intensity increases according to the quadratic law as the $|\mathbf{k}|$ value increases from 0 [23]. Study of the related YbAlO₃ compound [24,25] disclosed the exotic magnetic quantum states in the rare-earth subsystem at ultralow temperatures. It should be noted that Yb³⁺ is a Kramers ion, the ground state of which is split into doublets; therefore, the pseudospin-1/2 model is applicable. Upon splitting of the ground state in non-Kramers ions, the latter can create various combinations of singlet, doublet, pseudodoublet, and other energy levels. The more complex picture of the energy states makes it difficult to describe the behavior of the
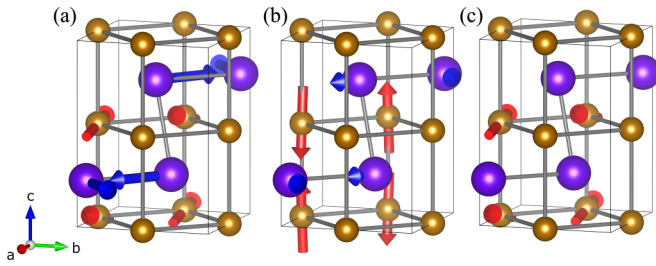
* Corresponding author: smp@iph.krasn.ru

FIG. 1. Schematic of the magnetic phases implemented in the TbFeO$_3$ single crystal at different temperatures. Brown and blue spheres indicate positions of Fe^{3+} and Tb^{3+} ions, respectively, and red and blue arrows show their average magnetic moments. (a) Phase below 3 K with the Fe^{3+} subsystem in the $\Gamma 4$ phase and the Tb^{3+} subsystem in the $\Gamma 8$ phase. In this phase, all the subsystems are ordered. (b) Transition phase between 3 and 8 K with the Fe^{3+} and Tb^{3+} subsystems in the $\Gamma 2$ phase. (c) Phase above 10 K up to T_N with the Fe^{3+} subsystem ordered in the $\Gamma 4$ phase and the disordered Tb^{3+} subsystem. The data presented are based on the results reported in [17].

rare-earth subsystem and the $3d$-$4f$ interaction between the sublattices, but the interesting effects and states expected in the compounds containing such ions broaden the scope for the development of physics of oxide materials.

Another compound studied by us was TmFeO$_3$ [26], in which the effect similar to the shadow mode was found in the rare-earth subsystem and the spin dynamics of the second singlet level was explored. The rare-earth subsystem was described in the approximation of an ion in an external field. We determined several parameters that can be used in the magnetic Hamiltonian, although, due to a variety of magnetic states of the Tm^{3+} ion, this was a challenge, both numerically and analytically.

In this study, to solve the problem of non-Kramers rare-earth ions in orthoferrites, the TbFeO$_3$ compound was investigated. This material orders at two temperatures: $T_N^{Fe} \approx$ 650 K and $T_N^{Tb} < 10$ K [17,19]. At the first ordering temperature, the iron subsystem is ordered antiferromagnetically, but with a weak DMI-induced ferromagnetic moment. This magnetic order is observed at temperatures from about 10 K; below 8 K, the compound undergoes a spin-reorientation transition. After that, the terbium subsystem starts ordering (see the schematic in Fig. 1). This compound was investigated by the techniques used previously to study the TmFeO$_3$ compound to better understand the physics of interactions in rare-earth orthoferrites.

II. EXPERIMENTAL DETAILS

The TbFeO$_3$ single crystal was grown in a Crystal Systems FZ-T-4000-H optical floating zone furnace (Japan) at a growth rate of 3 mm/h and a relative rod rotation at 30 rpm in air under ambient pressure. A sample $5 \times 5 \times 5$ mm^3 in size was cut from the grown rod along its crystallographic axes. The quality of the single crystal was estimated by the Laue method. Lauegrams and a photograph of the grown crystal are presented in Fig. 2.

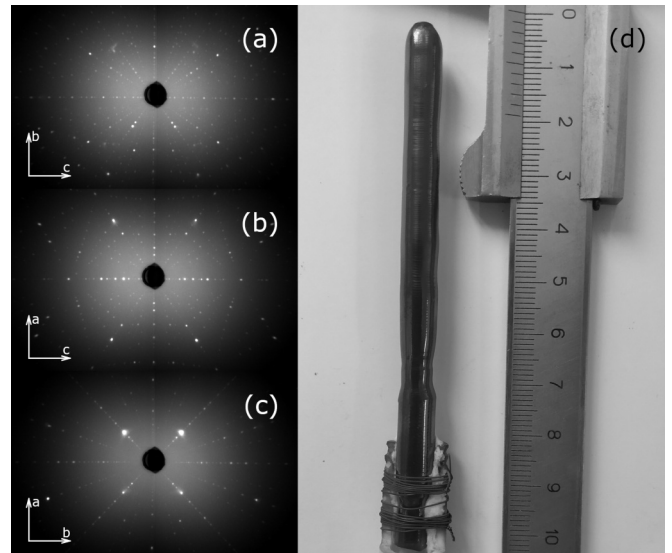The magnetic measurements were performed on a Quantum Design PPMS-6000 Physical Property Measurement

FIG. 2. (a)–(c) Lauegrams of the TbFeO$_3$ single crystal along different crystallographic directions corresponding to sp. gr. *Pbnm* with lattice parameters of $a = 5.326$ Å, $b = 5.602$ Å, and $c = 7.635$ Å. (d) Photograph of the single crystal obtained by optical floating zone melting.

System. The temperature and field dependencies of the magnetization were measured along different crystallographic directions in the single-crystal sample.

The $M(T)$ dependencies shown in Fig. 3 reveal a spin-reorientation transition in the temperature range of 3.5–8 K. In [17], this transition was identified as the $\Gamma 2$ phase, which confirmed the results reported in [27]. The slightly rounded,
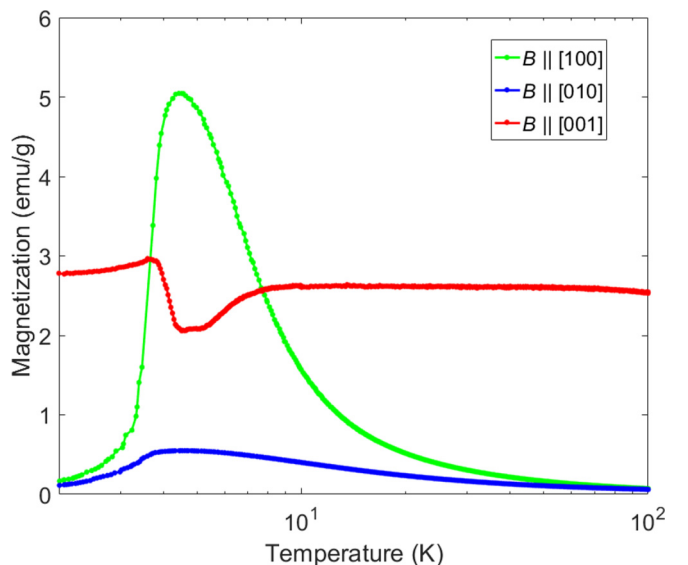
FIG. 3. Logarithmic temperature dependence of the magnetization. The measurements were performed at temperatures from 2 to 100 K after precooling the sample to 2 K in zero magnetic field. At 2 K, the hysteresis was measured in fields of ± 5 T; after that, the field was decreased to 0.01 T and the temperature dependence of the magnetization was measured. Of particular interest is the temperature range of 3.5–8 K corresponding to the spin-reorientation transition.

unsharp form of the curves can be explained by the difference between the experimental techniques used. It is noteworthy that the INS experiment used to draw the main conclusions in this work was carried out at $T = 2$ K, i.e., below the temperature of the spin-reorientation transition.

To analyze comprehensively the iron and terbium subsystem excitations in the $TbFeO_3$ single crystal, the INS study was carried out over wide reciprocal space and transferred energy ranges. The experiments were conducted using two time-of-flight neutron spectrometers: an angular-range chopper spectrometer (ARCS) [28] and a cold neutron chopper spectrometer (CNCS) [29,30] at the Oak Ridge National Laboratory's Spallation Neutron Source. The data were obtained on a single crystal with a mass of 3 g oriented in the $(0KL)$ scattering plane. The incident neutron energies were $E_i = 100$ and 25 meV for the ARCS and $E_i = 12$ and 3.3 meV for the CNCS.

The experimental data were processed and preliminarily analyzed using the Dave [31], Horace [32], and MantidPlot [33] software. The excitation spectra and neutron scattering cross sections of the spin Hamiltonian were calculated within the linear spin wave theory (LSWT) in the SpinW software package [34]. The crystal electric field (CEF) was calculated using the McPhase software [35].

III. RESULTS AND ANALYSIS

A. Iron subsystem

In this section we analyze the data obtained on the high-energy time-of-flight ARCS at incident neutron energies of 150 and 50 meV. The cuts along the highly symmetric directions of the reciprocal space reveal the magnon dispersion, which attains its maximum energy of 60 meV and can be considered with confidence to be the dispersion of the iron subsystem [22,26,36,37]. The low-energy region was investigated at neutron energies of up to 25 meV, which made it possible to examine the antiferromagnetic gap of the iron subsystem and determine the general characteristics of the rare-earth subsystem.

Based on the experimental data, we found positions of the curves at 72 points of the reciprocal space along the three highly symmetric directions in order to determine the spin Hamiltonian. The main challenge was to find an error of the selected points. The attempt to describe the selected points by the Gaussian function did not yield objective results because of the low density of points in the investigated ranges and a large error. Therefore, we used another model to determine an error of the points. The iterative algorithm was used, which compared intensity I_1 of a selected point with intensities of its neighbors in the chosen Q or E direction, depending on a cut. If the ratio between the intensity I_1 of a selected point and its neighbor's intensity I_2 was less than a chosen value, the process was repeated for the next neighbors with the accumulation of error factor n; otherwise, the solution was considered to be found and an error equal to 1/2 of the step in the cut direction $\cdot n$ was assigned to the value.

The behavior of the iron subsystem was described using the SpinW software package [34] and the classical spin Hamilto-

TABLE I. Stable exchange solutions for the iron subsystem.

	J_{ab} (meV)	J_c (meV)	J_{2ab} (meV)	J_{2c} (meV)	K_c (meV)
First	4.74	4.96	0.02	0.2	−0.02
Second	4.73	4.30	0.02	0.08	−0.02

nian [38]:

$$H = \sum_{i,j} J_{i,j} S_i S_j + K_c \sum_i S_{c_i}^2 \qquad (1)$$

in which two terms were taken into account: the first term is the Heisenberg exchange interaction between neighboring ions and the second term is the effective anisotropy. The DMI induces the magnon mode splitting in the vicinity of the $\Gamma 2$ [21]; however, the CEF excitation in the terbium subsystem around 17 meV makes the signal noisy, so the DMI effect on the spin dynamics cannot be reliably determined. The first summation is made over different sets of neighbors of Fe atoms. In Eq. (1), K_c is the effective anisotropy responsible for the $\Gamma 2$ phase stabilization. The exchange interaction model used by us is similar to that chosen in [26]; the in-plane and out-of-plane exchanges are separated. By fitting the model to experimental points, we found exchange values of $J_{ab} = 4.74$ meV, $J_c = 4.96$ meV, $J_{ab2} = 0.02$ meV, and $J_{c2} = 0.2$ meV, an anisotropy value of $K_c = -0.02$ meV, and deviations of $R_w = 2.51$.

In addition, this approach allowed us to get rid of the nonrepresentativeness of errors, but required the more thorough selection of fitting results in the physical model used. This was expressed in the variance of the solutions found; specifically, two stable solutions appeared with R_w 2.51% and 2.50% (see Table I). The analysis of our data can be considered satisfactory, since we managed to obtain the exchange values for the Fe^{3+} subsystem and thereby characterize the magnon dispersion in all the three directions of the reciprocal space (see Fig. 4). Good agreement between the experimental and calculated dispersions indicated the applicability of the LSWT-based model. In addition, the results on the iron subsystem obtained in this study are consistent with the data reported in [26].

B. Low-energy excitations

The rare-earth Tb^{3+} ion in the $TbFeO_3$ compound is a $4f$ element and its electrostatic interaction with surrounding ions can be described using Stevens operators. Terbium ions in $TbFeO_3$ have the monoclinic local symmetry C_s, which yields 15 nonzero operators that should be taken into account in the Hamiltonian [39]:

$$H_{cef} = \sum_{l,m} B_l^m O_l^m. \qquad (2)$$

These CEF parameters can be determined using the point charge model (PCM). The experience in using this model was demonstrated in [21,33]. In the PCM, atoms localized in a selected unit volume are considered to be point charges at crystallographic sites; this environment affects electrically the selected ion (in our case, Tb^{3+}) and, in this approach, any special interactions, spin parameters, etc. are ignored. We
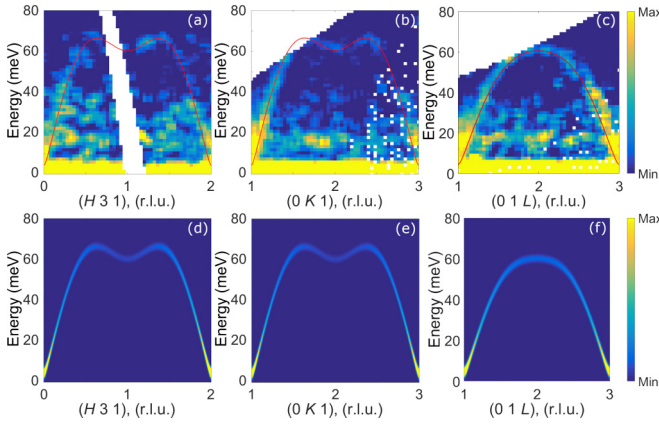
FIG. 4. Cuts along the three characteristic directions of the reciprocal space. (a)–(c) Experimental INS spectra recorded at a temperature of 2 K. The data were obtained by summation of the symmetric directions and smoothed with a Gaussian. The integration limit is ±0.1 r.l.u. The calculated dispersion curves (red) are superimposed. (d)–(f) Model calculation of the spectra within the selected model.

investigated neighboring ions lying within a sphere with a radius of $r = 4$ Å and calculated the parameters B_l^m (a set of the calculated B_l^m values is given in Table II of the Appendix) in the McPhase software package. Using the set of parameters, the CEF splitting, transition intensities, and magnetic anisotropy were simulated. The magnetization calculated using the obtained operators is shown in Fig. 5. It can be seen that the experimental and calculated data for all three directions are in satisfactory agreement. The experimental magnetizations are consistent with the data reported in [26] and the comparison of the calculated and experimental curves confirms the applicability of the PCM in describing the magnetization evolution in rare-earth orthoferrites reported previously in [22,26]. In addition, it should be noted that the calculated data describe satisfactorily the $M(H)$ anisotropy, even with disregard of the magnetic contribution of the iron subsystem.

Based on the parameters calculated using the PCM, the transition energies for the Tb^{3+} ion were simulated. The ground state of this ion is degenerate and consists of 13 states, 6 of which are quasidoublets and one is a singlet (a set of parameters is presented in the Appendix). The first calculated quasidoublet has an energy of $E_{0,1} \sim 0$ meV; this

TABLE II. Calculation of Stevens parameters B_l^m and energy levels with corresponding magnetic moments.

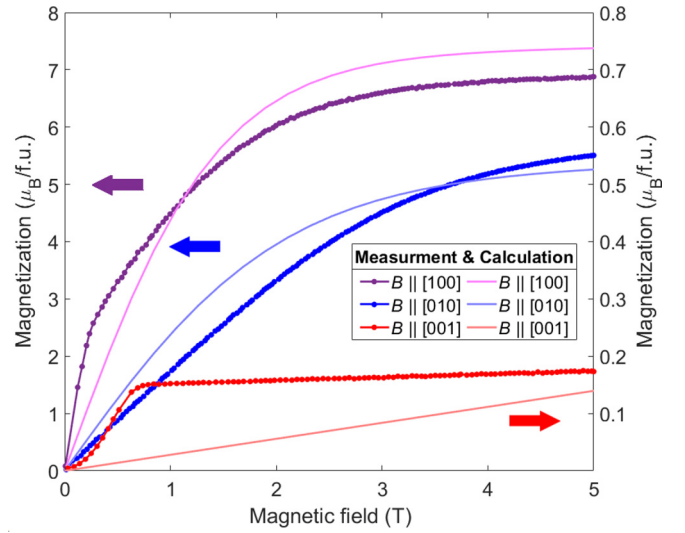| B_l^m	B_l^m
$B_2^0 = 3.91 \times 10^{-1}$	$B_6^0 = 0.1 \times 10^{-5}$
$B_2^2 = 0.39 \times 10^{-1}$	$B_6^2 = -0.3 \times 10^{-5}$
$B_2^{-2} = -3.03 \times 10^{-1}$	$B_6^{-2} = -0.3 \times 10^{-5}$
$B_4^0 = -0.35 \times 10^{-3}$	$B_6^4 = 1.8 \times 10^{-5}$
$B_4^2 = -1.34 \times 10^{-3}$	$B_6^{-4} = 0.1 \times 10^{-5}$
$B_4^{-2} = -3.37 \times 10^{-3}$	$B_6^6 = -0.3 \times 10^{-5}$
$B_4^4 = 0.45 \times 10^{-3}$	$B_6^{-6} = -0.0 \times 10^{-5}$
$B_4^{-4} = -8.1 \times 10^{-3}$	

FIG. 5. Magnetization vs magnetic field at 7 K. The green, blue, and red curves correspond to the [100], [010], and [001] crystallographic directions, respectively. Lines with dots show the experiment, and solid lines the calculation. The magnetization data for the [100] and [010] directions are plotted along the left-hand axis and the data for the [001] direction, along the right-hand axis.

level belongs to the elastic neutron spectrum. The second CEF level can be easily determined from the experimental data and located at 17 meV; in the calculation, this level is represented by a quasidoublet with $E_{2,3} \sim 14$ meV. Figures 6(a) and 6(b) show these energy levels together with the overlying levels corresponding to the quasidoublets calculated using the PCM. Figure 6(c) compares the calculated neutron dispersion intensities and the results of summation of the experimental data in the vicinity of the region [0, 2, 1]. The integration limit is ±0.25 r.l.u.

Having considered the energy range below 3.3 meV, we studied the magnetic excitations in the Tb subsystem and determined the correlation lengths in the two directions. The intensity cuts of the detected elastic peaks are shown in
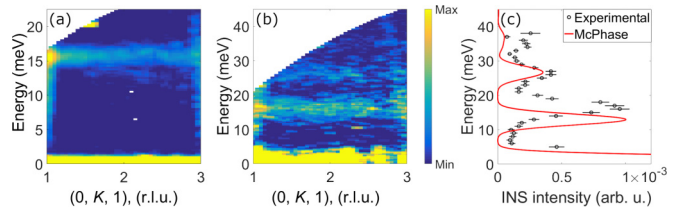

FIG. 6. (a) and (b) Cuts along the highly symmetric directions. The measurements were performed at 2 K. The data were obtained by summation of the symmetric directions. The integration limit is ±0.1 r.l.u. The spread operation was also used. The CEF level at 16–17 meV can be clearly seen in (a). In (b), there are two crystal field levels at 16–17 and 26 meV; around 34 meV, there is a hint of another CEF level, but it cannot be established with confidence. (c) Comparison of the integral CEF values with the calculation within the single-ion model in the McPhase software. The experimental data and the spin dynamics calculated using the PCM are in good agreement. The integration limit is ±0.25 r.l.u.
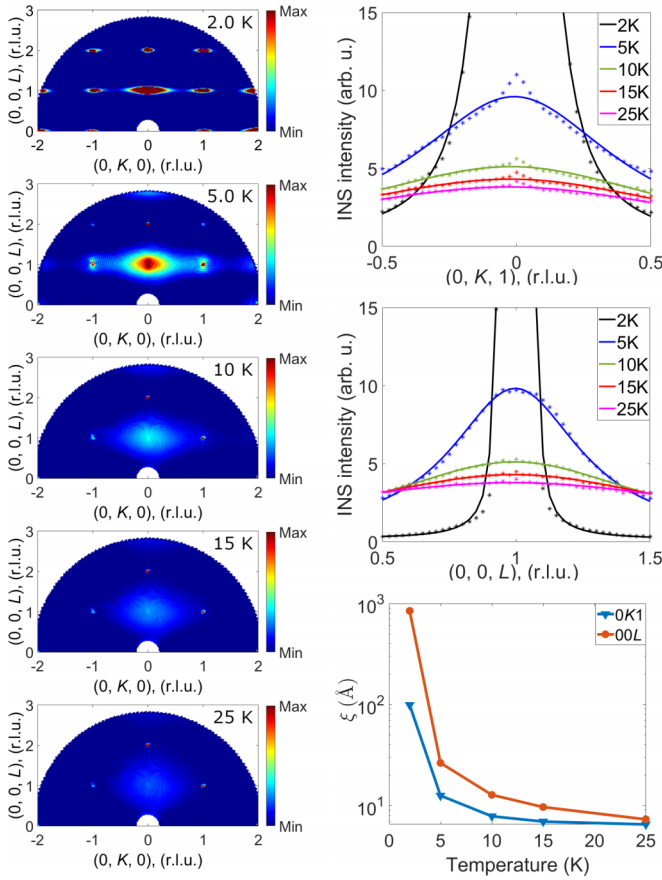
FIG. 7. (a) Experimental data integrated over the *H* directions of the reciprocal space in the limit ±0.1 r.l.u. The energy axis was integrated within ±0.1 meV. The cuts made at different temperatures in ascending order are arranged from up to down. (b) Experimental data integrated over the directions of the reciprocal space in the limit ±0.15 r.l.u. The energy axis was integrated within ±0.1 meV. Result of the approximation of the experimental data by the convolution of the Lorentzian and Gaussian functions. The resolution was estimated from the structural peak width using two characteristic directions of the reciprocal space. The temperature dependence of the correlation length for both directions of the reciprocal space is shown at the bottom.

Fig. 7(a). Study of the low-energy spectra at the diffuse scattering allowed us to describe the magnetic structure factor. Here, as in [40,41], we used the Lorentzian function

$$S(Q) \propto \frac{\sinh(c/\xi_l)}{\cosh(c/\xi_l) - \cos[\pi(l-1)]} \frac{\sinh(c/\xi_k)}{\cosh(c/\xi_k) - \cos[\pi k]}, \tag{3}$$

where ξ_l and ξ_k are the correlation lengths along the *c* and *b* axes, respectively.

Making the energy cuts in the *K* and *L* directions of the reciprocal space, we obtained the data shown by dots in Fig. 7(b). The approximation of the experimental data using the structural peak width and the Lorentzian function yielded the correlation lengths for each direction and temperature. The temperature dependence of the correlation length for the two investigated directions is also presented in Fig. 7(b). It can be clearly seen that, after the spin-reorientation transition, the correlation length sharply increases, which is consistent with the ordering of both subsystems below this transition.

TABLE III. The energy levels and out of ground state transition probabilities.

	E (meV)	$\langle n|J_x|m\rangle^2$	$\langle n|J_y|m\rangle^2$	$\langle n|J_z|m\rangle^2$
$|E_0\rangle \rightarrow |E_1\rangle$	0.0169	0.0	0.0	35.0109
$|E_0\rangle \rightarrow |E_2\rangle$	13.9161	0.0	3.0388	0.1414
$|E_0\rangle \rightarrow |E_3\rangle$	14.1608	0.8099	0.0	0.0
$|E_0\rangle \rightarrow |E_4\rangle$	24.7651	1.1200	0.0	0.0
$|E_0\rangle \rightarrow |E_5\rangle$	25.7851	0.0	1.4517	0.0658
$|E_0\rangle \rightarrow |E_6\rangle$	34.3537	0.0	0.0881	0.0154
$|E_0\rangle \rightarrow |E_7\rangle$	34.7824	0.325	0.0	0.0
$|E_0\rangle \rightarrow |E_8\rangle$	39.0313	0.0	0.0019	0.0052
$|E_0\rangle \rightarrow |E_9\rangle$	43.7716	0.0011	0.0	0.0
$|E_0\rangle \rightarrow |E_{10}\rangle$	44.4169	0.0319	0.0	0.0
$|E_0\rangle \rightarrow |E_{11}\rangle$	53.4470	0.0	0.0013	0.0007
$|E_0\rangle \rightarrow |E_{12}\rangle$	53.4992	0.0	0.0007	0.0003

IV. DISCUSSION AND CONCLUSION

The INS study of the single-crystal $TbFeO_3$ sample revealed the antiferromagnetic ordering of the Fe^{3+} subsystem. Using the spectra obtained, the Fe-Fe exchange interaction values were calculated within the linear spin wave theory. The spectra are similar to the spectra for iron in the $TmFeO_3$ compound from [26], which manifests itself in the energy levels of the magnon dispersion, in the exchange interaction values, and, importantly, in the anisotropy of the exchange values determined for these compounds.

The analysis of the spectra in the range of up to 50 meV elucidated the behavior of the Tb^{3+} subsystem, specifically, the position of the first three CEF levels, which are located at energies of 17, 25, and 35 meV for the compound under study. The data reported in this work do not show the magnon dispersion of these levels because of the insufficient resolution of the spectrometer in the investigated energy range. The splitting for the Tb^{3+} ion in the compound under study should be tenths of meV.

The magnetic subsystem of the rare-earth Tb^{3+} ion was described using the point charge model. In this model, the magnetization of the terbium subsystem and the CEF levels were calculated and plotted. The comparison of the calculation with the experiment demonstrated their good agreement. The correlation lengths at different temperatures were determined, which made it possible to establish the temperature below which the terbium subsystem acquires a long-range magnetic order.

APPENDIX: RESULTS OF THE POINT-CHARGE MODEL CALCULATIONS

The set of CEF parameters and the energy levels calculated from the PC model are given in Tables II and III, respectively.

[1] M. B. Salamon and M. Jaime, The physics of manganites: Structure and transport, Rev. Mod. Phys. **73**, 583 (2001).

[2] Y. Tokura and Y. Tomioka, Colossal magnetoresistive manganites, J. Magn. Magn. Mater. **200**, 1 (1999).

[3] H. Kimura, S. Kobayashi, Y. Fukuda, T. Osawa, Y. Kamada, Y. Noda, I. Kagomiya, and K. Kohn, Spiral spin structure in the commensurate magnetic phase of multiferroic RMn_2O_5, J. Phys. Soc. Jpn. **76**, 074706 (2007).

[4] M. Schieber, A. Grill, I. Nowik, B. M. Y. Wanklyn, R. C. Sherwood, and L. G. Van Uitert, Magnetocrystalline anisotropy of rare-earth manganites, J. Appl. Phys. **44**, 1864 (1973).

[5] C. Ritter, A. Vorotynov, A. Pankrats, G. Petrakovskii, V. Temerov, I. Gudim, and R. Szymczak, Magnetic structure in iron borates $RFe_3(BO_3)_4$ (R=Y, Ho): A neutron diffraction and magnetization study, J. Phys.: Condens. Matter **20**, 365209 (2008).

[6] A. I. Pankrats *et al.*, Transformation from an easy-plane to an easy-axis antiferromagnetic structure in the mixed rare-earth ferroborates $Pr_xY_{1-x}Fe_3(BO_3)_4$: Magnetic properties and crystal field calculations, J. Phys.: Condens. Matter **28**, 396001 (2016).

[7] A. S. Krylov *et al.*, Manifestation of magnetoelastic interactions in Raman spectra of $Ho_xNd_{1-x}Fe_3(BO_3)_4$ crystals, J. Adv. Dielect. **08**, 1850011 (2018).

[8] A. Pankrats, G. Petrakovskii, A. Kartashev, E. Eremin, and V. Temerov, Low-temperature magnetic phase diagram of $HoFe_3(BO_3)_4$ holmium ferroborate: A magnetic and heat capacity study, J. Phys.: Condens. Matter **21**, 436001 (2009).

[9] R. L. White, Work on the magnetic and spectroscopic properties of the rare-earth orthoferrites, J. Appl. Phys. **40**, 1061 (1969).

[10] I. Sosnowska and A. K. Zvezdin, Origin of the long period magnetic ordering in $BiFeO_3$, J. Magn. Magn. Mater. **140-144**, 167 (1995).

[11] B. Ruette, S. Zvyagin, A. P. Pyatakov, A. Bush, J. F. Li, V. I. Belotelov, A. K. Zvezdin, and D. Viehland, Magnetic-field-induced phase transition in $BiFeO_3$ observed by high-field electron spin resonance: Cycloidal to homogeneous spin order, Phys. Rev. B **69**, 064114 (2004).

[12] K. P. Belov, A. K. Zvezdin, and A. A. Mukhin, Magnetic phase transitions in terbium orthoferrite, J. Exp. Theor. Phys. **49**, 557 (1979).

[13] Y. Tokunaga, N. Furukawa, H. Sakai, Y. Taguchi, T. H. Arima, and Y. Tokura, Composite domain walls in a multiferroic perovskite ferrite, Nat. Mater. **8**, 558 (2009).

[14] A. V. Kimel, A. Kirilyuk, P. A. Usachev, R. V. Pisarev, A. M. Balbashov and Th. Rasing, Ultrafast non-thermal control of magnetization by instantaneous photomagnetic pulses, Nature (London) **435**, 655 (2005).

[15] J. A. de Jong, A. V. Kimel, R. V. Pisarev, A. Kirilyuk, and Th. Rasing, Laser-induced ultrafast spin dynamics in $ErFeO_3$, Phys. Rev. B **84**, 104421 (2011).

[16] J. Jiang, Z. Jin, G. Song, X. Lin, G. Ma, and S. Cao, Dynamical spin reorientation transition in $NdFeO_3$ single crystal observed with polarized terahertz time domain spectroscopy, Appl. Phys. Lett. **103**, 062403 (2013).

[17] S. Artyukhin, M. Mostovoy, N. P. Jensen, D. Le, K. Prokes, V. G. de Paula, H. N. Bordallo, A. Maljuk, S. Landsgesell, H. Ryll, B. Klemke, S. Paeckel, S. Kiefer, K. Lefmann, L. T. Kuhn, and D. N. Argyriou, Solitonic lattice and Yukawa forces in the rare-earth orthoferrite $TbFeO_3$, Nat. Mater. **11**, 694 (2012).

[18] K. Saito, A. Sato, A. Bhattacharjee, and M. Sorai, High-precision detection of the heat-capacity anomaly due to spin reorientation in $TmFeO_3$ and $HoFeO_3$, Solid State Commun. **120**, 129 (2001).

[19] O. Nikolov, I. Hall, S. N. Barilo, and S. A. Guretskii, A Mossbauer study of temperature-driven spin-reorientation transitions in $TbFeO_3$, J. Phys.: Condens. Matter **6**, 3793 (1994).

[20] I. E. Dzialoshinskii, Thermodynamic theory of weak ferromagnetism in antiferromagnetic substances, Sov. Phys. JETP-USSR **5**, 1259 (1957).

[21] A. Podlesnyak, S. E. Nikitin, and G. Ehlers, Low-energy spin dynamics in rare-earth perovskite oxides, J. Phys.: Condens. Matter **33**, 403001 (2021).

[22] S. E. Nikitin, L. S. Wu, A. S. Sefat, K. A. Shaykhutdinov, Z. Lu, S. Meng, E. V. Pomjakushina, K. Conder, G. Ehlers, M. D. Lumsden, A. I. Kolesnikov, S. Barilo, S. A. Guretskii, D. S. Inosov, and A. Podlesnyak, Decoupled spin dynamics in the rare-earth orthoferrite $YbFeO_3$: Evolution of magnetic excitations through the spin-reorientation transition, Phys. Rev. B **98**, 064424 (2018).

[23] I. Cabrera, J. D. Thompson, R. Coldea, D. Prabhakaran, R. I. Bewley, T. Guidi, J. A. Rodriguez-Rivera, and C. Stock, Excitations in the quantum paramagnetic phase of the quasi-one-dimensional Ising magnet $CoNb_2O_6$ in a transverse field: Geometric frustration and quantum renormalization effects, Phys. Rev. B **90**, 014418 (2014).

[24] L. S. Wu, S. E. Nikitin, Z. Wang, W. Zhu, C. D. Batista, A. M. Tsvelik, A. M. Samarakoon, D. A. Tennant, M. Brando, L. Vasylechko, M. Frontzek, A. T. Savici, G. Sala, G. Ehlers, A. D. Christianson, M. D. Lumsden, and A. Podlesnyak, Tomonaga-Luttinger liquid behavior and spinon confinement in $YbAlO_3$, Nat. Commun. **10**, 698 (2019).

[25] S. E. Nikitin, S. Nishimoto, Y. Fan, J. Wu, L. S. Wu, A. S. Sukhanov, M. Brando, N. S. Pavlovskii, J. Xu, L. Vasylechko, R. Yu and A. Podlesnyak, Multiple fermion scattering in the weakly coupled spin-chain compound $YbAlO_3$, Nat. Commun. **12**, 1 (2021).

[26] S. A. Skorobogatov, S. E. Nikitin, K. A. Shaykhutdinov, A. D. Balaev, K. Yu. Terentjev, G. Ehlers, G. Sala, E. V. Pomjakushina, K. Conder, and A. Podlesnyak, Low-temperature spin dynamics in the $TmFeO_3$ orthoferrite with a non-Kramers ion, Phys. Rev. B **101**, 014432 (2020).

[27] Y. Cao, M. Xiang, W. Zhao, G. Wang, Z. Feng, B. Kang, A. Stroppa, J. Zhang, W. Ren, and S. Cao, Magnetic phase transition and giant anisotropic magnetic entropy change in $TbFeO_3$ single crystal, J. Appl. Phys. **119**, 063904 (2016).

[28] D. L. Abernathy, M. B. Stone, M. J. Loguillo, M. S. Lucas, O. Delaire, X. Tang, J. Y. Y. Lin, and B. Fultz, Design and operation of the wide angular-range chopper spectrometer ARCS at the Spallation Neutron Source, Rev. Sci. Instrum. **83**, 015114 (2012).

[29] G. Ehlers, A. A. Podlesnyak, J. L. Niedziela, E. B. Iverson, and P. E. Sokol, The new cold neutron chopper spectrometer at the spallation neutron source: Design and performance, Rev. Sci. Instrum. **82**, 085108 (2011).

[30] G. Ehlers, A. Podlesnyak, and A. I. Kolesnikov, The cold neutron chopper spectrometer at the Spallation Neutron Source - A review of the first 8 years of operation, Rev. Sci. Instrum. **87**, 093902 (2016).

[31] R. Azuah, L. Kneller, Y. Qiu, P. Tregenna-Piggott, C. Brown, J. Copley, and R. Dimeo, DAVE: A comprehensive software suite for the reduction, visualization, and analysis of low energy neutron spectroscopic data, J. Res. Natl. Inst. Stand. Technol. **114**, 341 (2009).

[32] R. A. Ewings, A. Butsa, M. D. Lea, J. van Duijnb, I. Bustinduyc, and T. G. Perring, HORACE: Software for the analysis of data from single crystal spectroscopy experiments at time-of-light neutron instruments, Nucl. Instrum. Methods Phys. Res. Sect. A **834**, 132 (2016).

[33] O. Arnold, J. C. Bilheux, J. M. Borreguero, A. Buts, S. I. Campbell, L. Chapon, M. Doucet, N. Draper, R. Ferraz Leal, M. A. Gigg, V. E. Lynch, A. Markvardsen, D. J. Mikkelsone, R. L. Mikkelsone, R. Miller, K. Palmen, P. Parker, G. Passos, T. G. Perring, P. F. Peterson, S. Ren *et al.*, Mantid - Data analysis and visualization package for neutron scattering and μSR experiments, Nucl. Instrum. Methods Phys. Res. Sect. A **764**, 156 (2014).

[34] S. Toth and B. Lake, Linear spin wave theory for single-Q incommensurate magnetic structures, J. Phys.: Condens. Matter **27**, 166002 (2015).

[35] M. Rotter, Using McPhase to calculate magnetic phase diagrams of rare earth compounds, J. Magn. Magn. Mater. **272-276**, E481 (2004).

[36] S. E. Hahn, A. A. Podlesnyak, G. Ehlers, G. E. Granroth, R. S. Fishman, A. I. Kolesnikov, E. Pomjakushina, and K. Conder, Inelastic neutron scattering studies of $YFeO_3$, Phys. Rev. B **89**, 014420 (2014).

[37] S. M. Shapiro, J. D. Axe, and J. P. Remeika, Neutronscattering studies of spin waves in rare-earth orthoferrites, Phys. Rev. B **10**, 2014 (1974).

[38] To stabilize the correct ground state with a small spin canting [9] we have to introduce two Dzyaloshinskii-Moriya interaction constants to Eq. (1). However, both are small and have a negligible effect of the spectra.

[39] M. T. Hutchings, Point-charge calculations of energy levels of magnetic ions in crystalline electric fields, Solid State Phys. **16**, 227 (1964).

[40] I. Zaliznyak, A. T. Savici, M. Lumsden, A. Tsvelik, R. Hu, and C. Petrovic, Spin-liquid polymorphism in a correlated electron system on the threshold of superconductivity, Proc. Natl. Acad. Sci. USA **112**, 10316 (2015).

[41] L. S. Wu, S. E. Nikitin, M. Frontzek, A. I. Kolesnikov, G. Ehlers, M. D. Lumsden, K. A. Shaykhutdinov, E.-J. Guo, A. T. Savici, Z. Gai, A. S. Sefat, and A. Podlesnyak, Magnetic ground state of the Ising-like antiferromagnet $DyScO_3$, Phys. Rev. B **96**, 144407 (2017).